


Cite this: *J. Mater. Chem. A*, 2019, 7, 13205

Oxygen vacancy-enriched MoO_{3-x} nanobelts for asymmetric supercapacitors with excellent room/low temperature performance†

Qi-Long Wu,^{ab} Shi-Xi Zhao,^{ab} *^a Le Yu,^{ab} Xiao-Xiao Zheng,^{ab} Yi-Feng Wang,^{ab} Lü-Qiang Yu,^{ab} Ce-Wen Nan^b and Guozhong Cao^{*c}

Oxygen vacancy-enriched MoO_{3-x} nanobelts with oxygen vacancies up to 20% (equal to MoO_{2.4}) were synthesized and demonstrated fast reaction kinetics. An asymmetric supercapacitor was assembled with active carbon (AC) as the anode and the as-prepared MoO_{3-x} nanobelts as the cathode. A new aqueous electrolyte of H₂SO₄/ethylene glycol (EG) was investigated and found to work appropriately at low temperatures, even at -25 °C. The MoO_{3-x} nanobelts electrode possesses excellent specific capacitance, rate capacity (1230 F g⁻¹ and 1220 F g⁻¹ at 5 A g⁻¹ and 50 A g⁻¹, respectively) and cycle performance (100% after 38 000 cycles). Its energy and power densities reached 111 W h kg⁻¹ and 803 W kg⁻¹ or 50 W h kg⁻¹ and 27 321 W kg⁻¹ and maintained 80 W h kg⁻¹ and 794 W kg⁻¹ or 17 W h kg⁻¹ and 23 565 W kg⁻¹ at -25 °C. It is hypothesized that the coexistence of oxygen vacancies and low valence Mo ions enhanced both mass and charge transport kinetics and catalyzed the redox reactions.

Received 2nd April 2019
Accepted 29th April 2019

DOI: 10.1039/c9ta03471d

rsc.li/materials-a

1. Introduction

In recent decades, supercapacitors, as a type of device in the field of energy storage and conversion, have received increasing attention^{1,2} due to their high power density, excellent cycle stability and good safety. Supercapacitors can be divided into two types: electrical double-layer capacitors (EDLCs) and pseudocapacitors on the basis of their energy storage mechanism. EDLCs mainly include carbon materials, which store charge by adsorbing ions in the electrolyte on the interface of electrode materials/electrolyte. The specific capacity depends much on the specific surface area of electrode materials, which is usually very low and cannot meet the requirements of development. Carbon materials for supercapacitors³ mainly contain active carbon,^{4,5} graphene⁶⁻⁸ and carbon nanotubes,^{9,10} which possess superhigh specific surface area. However, pseudocapacitors store charge by highly reversible redox reactions between electrode materials and electrolyte ions and their specific capacitance is much higher than that of EDLCs. Meanwhile, they can maintain high power density. So, pseudocapacitors have great potential to achieve high energy density and power density

which makes them promising to be the next generation of energy storage and conversion devices.¹¹ Many pseudocapacitive materials such as transition metal oxides/hydroxides (RuO₂,¹² MnO₂,¹³ NiO,¹⁴ and Ni(OH)₂¹⁵), transition metal sulfides (MoS₂)¹⁶⁻¹⁸ and conducting polymers (PANI and PPy)¹⁹⁻²² have been introduced and studied in the field of supercapacitors. These studies achieved high-performance pseudocapacitors, including specific capacitance/rate performance/cycle stability or their integrated performance. Even so, the energy density of supercapacitors is still lower than that of rechargeable lithium-ion batteries. The rate performance and cycle stability of pseudocapacitors are also unsatisfactory because of their unbecoming microstructures and poor electrical conductivity. The methods to improve the performance of pseudocapacitive materials can be summarized as follows:²³ (1) optimize the microstructures of electrode materials. *E.g.*, MnO₂ nanorods were deposited uniformly on the surface of graphene oxide. This can prevent the accumulation of MnO₂, which is beneficial for improving the speed of electron transportation and shortening the ion migration path.²⁴ (2) Increase the contact area between electrode materials and the electrolyte. (3) Explore new materials with high levels of active sites. *E.g.*, ultrathin porous nickel hydroxide-manganese dioxide hybrid nanosheets can achieve a high specific capacity of 2628 F g⁻¹ (3 A g⁻¹).¹⁵ However, these methods have not realized excellent integrated performance of specific capacitance, rate capacity and cycle stability. Introducing vacancies in transition metal oxides has been proved to be highly effective.²⁵ In this way, the overall electrical conductivity of electrode materials can be improved effectively. Coupled with optimized microstructures

^aGraduate School at Shenzhen, Tsinghua University, Shenzhen, 518055, China. E-mail: zhaosx@sz.tsinghua.edu.cn

^bSchool of Materials Science and Engineering, Tsinghua University, Beijing, 100084, China

^cDepartment of Materials Science and Engineering, University of Washington, Seattle, WA 98195, USA. E-mail: gzcao@uw.edu

† Electronic supplementary information (ESI) available. See DOI: 10.1039/c9ta03471d

of electrode materials, excellent integrated performance is likely to be achieved. Moreover, aqueous electrolytes for supercapacitors usually cannot tolerate low temperatures below 0 °C, constraining the application of aqueous supercapacitors. Therefore, it is quite meaningful to research aqueous electrolytes that can tolerate low temperatures.

Mo-based oxides/sulfides show high electrochemical activity due to their multiple valences, and possess great potential in the field of energy storage and conversion.²⁶ Among these oxides/sulfides, MoO₃ has significant advantages in various aspects such as a simple preparation process, high electrochemical activity, high theoretical specific capacitance, good thermal and mechanical stability, low cost and being friendly to the environment. However, studies have been far from adequate for MoO₃. The research performed on MoO₃ mainly involves (1) compositing with carbon materials (*e.g.* active carbon, graphene, and carbon nanotubes).^{27–30} (2) Compositing with conducting polymers (*e.g.* polyaniline and polypyrrole).^{20,31,32} (3) Reducing some Mo⁶⁺ to a lower valence (Mo⁵⁺, Mo⁴⁺ or Mo³⁺).^{33–36} Although these studies have reported some achievements and breakthroughs, the essential issues have not been solved to achieve excellent integrated performance. The leading reasons can be concluded as follows: (1) these studies cannot achieve an entirely uniform combination between MoO₃ and carbon or other materials from a microscopic perspective because every phase of the composite still retains its own structure to a large extent. The composite exhibits integrated performance of its components only in its joints. (2) A good method is to reduce some MoO₃ because oxygen vacancies improve the intrinsic conductivity of MoO₃.^{37,38} But most studies in the past have focused on secondary reduction, namely, fully oxidized MoO₃ was prepared first, followed by chemical or thermal reduction to obtain some Mo⁵⁺ or Mo⁴⁺ in MoO₃. The disadvantage is that the reduction process can only be conducted on the surface and cannot extend to the inside of MoO₃. The performance improved by this method is also very limited.

Here, we put forward a simple one-step hydrothermal method that can directly grow ultrathin and narrow MoO_{3–x} nanobelts with rich oxygen vacancies. It is worth noting that Mo⁶⁺ was reduced from the interior to the exterior of MoO_{3–x} nanobelts. Mo⁶⁺, Mo⁵⁺ and Mo⁴⁺ in MoO_{3–x} nanobelts were

detected by X-ray photoelectron spectroscopy (XPS), which shows that the abundant oxygen vacancies distribute uniformly from the inside to the surface of MoO_{3–x} nanobelts. The mass of oxygen vacancies contributes a lot to their intrinsic conductivity. Coupled with the ultrathin and narrow microstructure, the MoO_{3–x} nanobelt electrode shows excellent performance in a H₂SO₄ electrolyte. To solve the problem of aqueous electrolytes being unable to tolerate low temperatures, we innovatively prepared a new H₂SO₄/ethylene glycol (EG) aqueous electrolyte that can tolerate a low temperature of –25 °C. MoO_{3–x} nanobelts realized high integrated performance in the H₂SO₄/EG electrolyte at different temperatures. This work is believed to promote the study and application of pseudocapacitive materials in the field of energy storage and conversion.

2. Experimental

2.1 Materials preparation

The schematic diagram of the preparation of MoO₃ and oxygen vacancy-enriched MoO_{3–x} nanobelts is presented in Fig. 1. They are both prepared by a simple one-step hydrothermal method and no other processes.

Synthesis of the MoO₃ nanobelts: typically, 0.48 g Mo powder was added into 10 mL H₂O₂ (30%) with vigorous stirring for about 5 minutes in an ice bath until the reaction was complete, and the mixture was cooled down. Then, 60 mL deionized water was added into the solution prepared above, followed by sustained stirring at 25 °C for 1 h. The mixed solution exhibited a luminous yellow color. The luminous yellow solution was transferred into a 100 mL Teflon-lined stainless steel autoclave and kept in an oven at 140 °C for 18 h. After the reaction was complete, the white precipitate was washed alternately with ethyl alcohol and deionized water three times. Finally, the as-prepared sample was dried at 80 °C for 12 h.

Synthesis of the oxygen vacancy-enriched MoO_{3–x} nanobelts: the preparation process was almost the same as that for the fully oxidized ultrathin MoO₃ nanobelts except the 60 mL deionized water was replaced with 10 mL ethyl alcohol and 50 mL deionized water. Ethyl alcohol plays the role of reducing Mo⁶⁺ to Mo⁵⁺ or Mo⁴⁺.³⁴ It is worth noting that the as-prepared sample

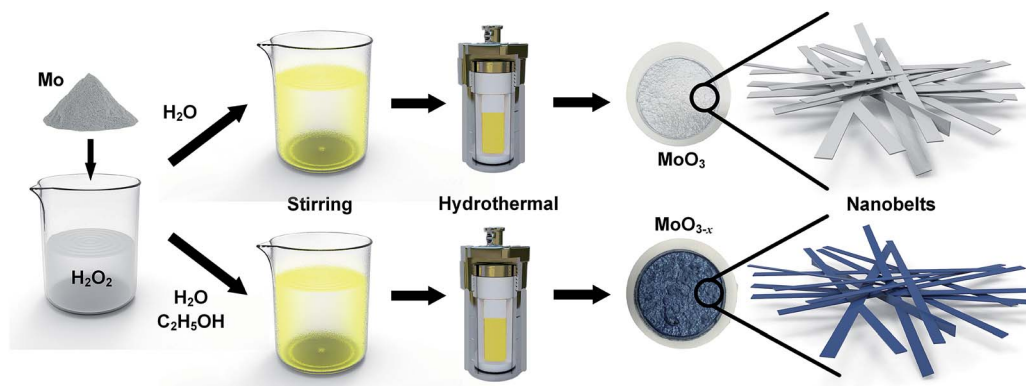


Fig. 1 Schematic illustration of the preparation process of MoO₃ and MoO_{3–x} nanobelts.

exhibited a dark blue color, indicating that some Mo^{6+} were reduced successfully in the hydrothermal process.

2.2 Preparation of the $\text{H}_2\text{SO}_4/\text{EG}$ aqueous low-temperature electrolyte

Generally speaking, aqueous electrolytes in supercapacitors cannot tolerate temperatures below $0\text{ }^\circ\text{C}$. Here, a type of low-temperature electrolyte (labelled $\text{H}_2\text{SO}_4/\text{EG}$) was prepared by first mixing concentrated H_2SO_4 , ethylene glycol (EG) and deionized water. The molarity of H_2SO_4 is 1 M and the volumetric fraction of EG is 30%. The corresponding room-temperature electrolyte is 1 M H_2SO_4 (labelled H_2SO_4). The performance of single MoO_{3-x} nanobelts shows no evident difference in the H_2SO_4 and $\text{H}_2\text{SO}_4/\text{EG}$ electrolytes. The asymmetric supercapacitor assembled with the $\text{H}_2\text{SO}_4/\text{EG}$ electrolyte exhibits excellent performance at $-25\text{ }^\circ\text{C}$, $0\text{ }^\circ\text{C}$ and $25\text{ }^\circ\text{C}$.

2.3 Materials characterization

The ultrathin MoO_3 and MoO_{3-x} nanobelts were characterized by X-ray diffraction (XRD, D8 Advance, $\text{Cu K}\alpha$, $\lambda = 0.15418\text{ nm}$, scan rate: 5° min^{-1}), Field-emission Scanning Electron Microscopy (FESEM, ZEISS SUPRA55), Field-emission Transmission Electron Microscopy (TEM, FEI Tecnai G2 F30), and X-ray photoelectron spectroscopy (XPS, PHI 5000 V VersaProbe), and using Brunauer–Emmett–Teller measurements (BET, BELSORP-Max, N_2 atmosphere) and a Contact Angle Meter (DSA30 $0\text{--}180^\circ$). Thermogravimetric Analysis (TGA, TGA2, N_2 atmosphere) was carried out between 25 and $1000\text{ }^\circ\text{C}$ with a heating rate of $5\text{ }^\circ\text{C min}^{-1}$ in a N_2 atmosphere. Argon plasma was used to etch MoO_{3-x} nanobelts to detect Mo^{4+} , Mo^{5+} and Mo^{6+} inside the MoO_{3-x} nanobelts in the XPS test.

2.4 Preparation of the MoO_3 and MoO_{3-x} electrodes

The active materials (MoO_3 or MoO_{3-x} nanobelts), acetylene black and PVDF in a mass ratio of $8 : 1 : 1$ were mixed with suitable NMP concentrations to obtain a uniform slurry. Then the slurry was painted on conductive carbon paper (current collector, 1 cm^2), followed by drying in a vacuum oven at $120\text{ }^\circ\text{C}$ for 12 h. The mass loading of active materials is about $1.5\text{--}1.8\text{ mg}$ for both the three-electrode and two-electrode systems.

2.5 Electrochemical characterization

Single electrode: a standard three-electrode test system was used to evaluate the properties of ultrathin MoO_3 and MoO_{3-x} nanobelt electrodes with a Pt plate as the counter electrode and a saturated calomel electrode as the reference electrode. For comparison, the MoO_3 nanobelt electrode was tested with the 1 M H_2SO_4 electrolyte. And for the MoO_{3-x} electrode, both H_2SO_4 and $\text{H}_2\text{SO}_4/\text{EG}$ were used as the electrolytes. Cyclic voltammetry (CV) and galvanostatic charge/discharge (GCD) tests were both performed in a voltage window of $-0.6\text{--}0.2\text{ V}$. Electrochemical impedance spectroscopy (EIS) was performed in a frequency range from 100 kHz to 0.01 Hz . Their cycle performances were measured under a high current density of 50 A g^{-1} .

The asymmetric supercapacitor was characterized in a two-electrode test system at different temperatures from $-25\text{--}25\text{ }^\circ\text{C}$. The anode was prepared using a mixture of active carbon (AC), acetylene black and PVDF with suitable NMP concentrations in a mass ratio of $8 : 1 : 1$. Conductive carbon paper was also used as the current collector of the anode. The cathode was the MoO_{3-x} electrode. In addition, based on the principle of charge balance between the two electrodes, the mass ratio of the AC and MoO_{3-x} electrodes is about $3 : 1$ which is calculated from their CV capacitance at 10 mV s^{-1} (Fig. 8a). Low-temperature electrochemical measurements of the single MoO_{3-x} electrode and the AC|| MoO_{3-x} asymmetric supercapacitor were carried out in a high–low temperature chamber (JK-80T).

All the electrochemical measurements mentioned above were performed with a Gamry (interface 1000, Germany) electrochemical workstation. The relevant calculation formulas for specific capacitance (C_s for single electrodes, C for the asymmetric supercapacitor), energy density (E) and power density (P) can be found in the ESI.†

3. Results and discussion

3.1 Structure and morphology

Fig. 1 shows the MoO_3 and MoO_{3-x} nanobelts prepared by the facile one-step hydrothermal process. Ethyl alcohol was used to reduce Mo^{6+} during MoO_{3-x} crystal growth. Mo^{5+} is blue. The as-prepared MoO_{3-x} nanobelts exhibit a unique dark blue color, quite different from that of MoO_3 nanobelts (white),

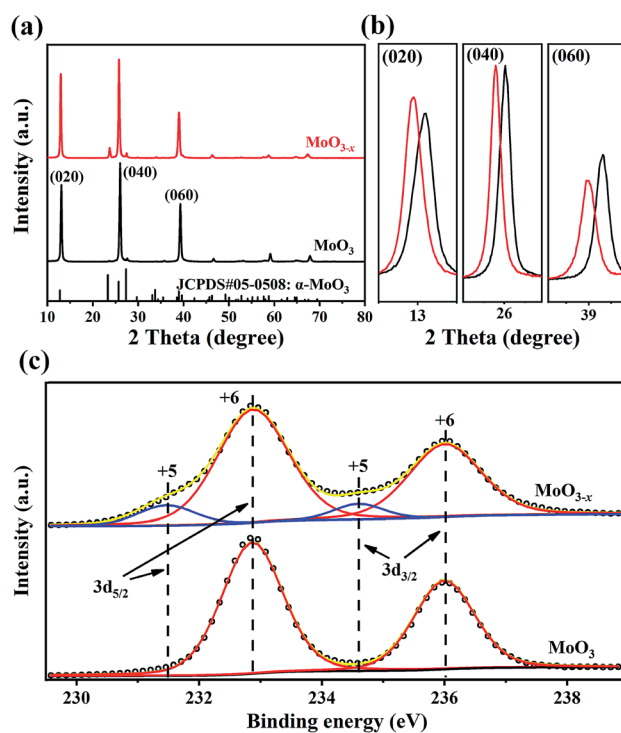


Fig. 2 (a) XRD patterns of MoO_3 and MoO_{3-x} nanobelts; (b) detailed view of the three main peaks in (a); (c) superficial XPS test results of MoO_3 and MoO_{3-x} nanobelts.

demonstrating that some Mo^{6+} were reduced to Mo^{5+} or Mo^{4+} by ethyl alcohol in the hydrothermal process.^{25,33}

Fig. 2a shows the XRD patterns of MoO_3 and MoO_{3-x} nanobelts, which match well with the standard card of JCPDS#05-0508 ($\alpha\text{-MoO}_3$) and indicate that there is no parasitic phase. It is also noted that there is hardly any peak except (020), (040) and (060), showing an obviously preferred orientation. Fig. 2b shows the detailed view of the three main peaks of MoO_3 and MoO_{3-x} nanobelts, from which it can be seen that the peaks of MoO_{3-x} nanobelts undergo a slight shift to smaller angles compared with those of MoO_3 nanobelts. Based on Bragg's law ($2d \sin \theta = \lambda$), the (020) interplanar spacing of MoO_{3-x} nanobelts was calculated to increase by about 1.11% compared to that of MoO_3 nanobelts. The superficial XPS spectra of MoO_3 and MoO_{3-x} nanobelts are shown in Fig. 2c. The peaks at 232.88 and 236.01 eV represent $\text{Mo}^{6+} 3d_{5/2}$ and $3d_{3/2}$, respectively; the peaks at 231.47 and 234.60 eV correspond to $\text{Mo}^{5+} 3d_{5/2}$ and $3d_{3/2}$, respectively. The amount of Mo^{5+} in the surface layer of MoO_{3-x} nanobelts was calculated to be $x = 0.063$, or 2.1% oxygen vacancy.

The SEM images of MoO_{3-x} and MoO_3 nanobelts are presented in Fig. 3a and S1,[†] respectively. The width of MoO_{3-x} nanobelts is about 100–200 nm (about 1/3 of that of MoO_3 nanobelts) and their thickness is about 35 nm. In addition, the dispersity of MoO_{3-x} nanobelts is much better than that of MoO_3 nanobelts (Fig. S1-b and S1-c[†]). Fig. 3b and c show the TEM images of MoO_{3-x} nanobelts; the length and width directions of MoO_{3-x} nanobelts correspond to the [200] and [002] directions, respectively. $\alpha\text{-MoO}_3$ is constituted by octahedra (Fig. 3d). Abundant 1-D and 2-D diffusion channels exist inside $\alpha\text{-MoO}_3$. 1-D diffusion channels are in the width direction of MoO_{3-x} nanobelts and 2-D diffusion channels are parallel to the (010) plane of MoO_{3-x} nanobelts. So, MoO_{3-x} nanobelts are easy to be infiltrated by the electrolyte, further contributing to the high utilization of active sites. TGA and BET test results of MoO_3 and MoO_{3-x} nanobelts can be found in Fig. S2-a and S2-b.[†] Both of them have a good thermal stability and can tolerate a high temperature of over 700 °C. MoO_{3-x}

nanobelts have a larger specific surface area of $18.54 \text{ m}^2 \text{ g}^{-1}$ than MoO_3 ($11.34 \text{ m}^2 \text{ g}^{-1}$).

Argon plasma was used to etch MoO_{3-x} nanobelts to detect Mo atoms with different valences inside MoO_{3-x} nanobelts. Fig. 4a shows the percentages of Mo^{4+} , Mo^{5+} and Mo^{6+} at different depths of MoO_{3-x} nanobelts and Fig. 4b–d exhibit the XPS spectra at depths of 0, 3, and 5 nm of MoO_{3-x} nanobelts, respectively (the XPS spectra of 8–25 nm can be found in Fig. S3[†]). The reason why the proportions of Mo^{4+} and Mo^{5+} in the surface are relatively low may be that most of the Mo^{4+} and Mo^{5+} were oxidized to Mo^{6+} in the vacuum filtration process in air. It is discovered that there are amounts of Mo^{4+} and Mo^{5+} with homogeneous distribution inside MoO_{3-x} nanobelts. The proportion of Mo^{4+} , Mo^{5+} and Mo^{6+} in MoO_{3-x} nanobelts remains almost constant from 5–25 nm. The x value in MoO_{3-x} can be calculated to be about 0.6, showing that MoO_{3-x} actually is $\text{MoO}_{2.4}$. Quantities of oxygen vacancies act as shallow donors and thus increase the concentration of the carrier,^{39,40} resulting in the improvement of electrical conductivity and faster reaction kinetics in the bulk. Moreover, oxygen vacancies also lead to the increase of interplanar spacing of MoO_{3-x} nanobelts in the [010] direction (increases about 1.1% calculated from their XRD patterns in Fig. 2a). The results discussed above are not similar to those of MoO_3 reduced in two steps,^{33,34,36} for which the method cannot obtain abundant oxygen vacancies and the oxygen vacancies are just on the surface of MoO_{3-x} . Their effects thus are quite limited in terms of the overall enhancement of performance for supercapacitors. However, the MoO_{3-x} nanobelts we synthesized exhibit excellent performance of specific capacitance, rate capacity, and cycle stability and outstanding low-temperature performance.

The aqueous $\text{H}_2\text{SO}_4/\text{EG}$ electrolyte was used for low temperature applications. Interestingly, the performance of MoO_{3-x} nanobelts shows no obvious difference between the H_2SO_4 and $\text{H}_2\text{SO}_4/\text{EG}$ electrolyte. The wettability of the H_2SO_4 and $\text{H}_2\text{SO}_4/\text{EG}$ electrolytes with MoO_3 and MoO_{3-x} nanobelts

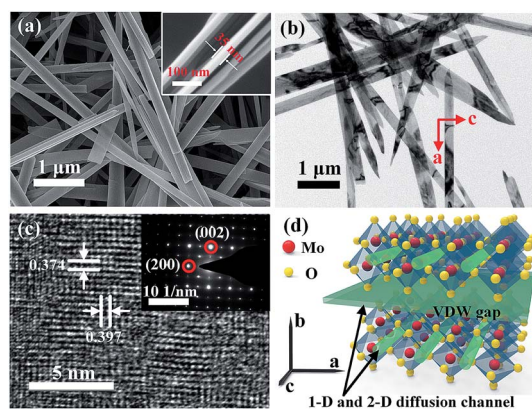


Fig. 3 (a) and (b) SEM and TEM images of MoO_{3-x} nanobelts; the inset in (a) shows the sectional view of MoO_{3-x} nanobelts; (c) HR-TEM image and SAED pattern (inset) of MoO_{3-x} nanobelts; (d) the crystal structure of $\alpha\text{-MoO}_3$.

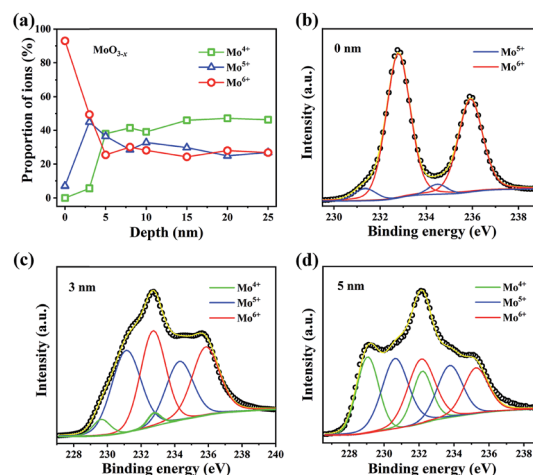


Fig. 4 (a) Proportion of Mo^{4+} , Mo^{5+} and Mo^{6+} at different depths of MoO_{3-x} nanobelts; (b), (c) and (d) XPS spectra of MoO_{3-x} nanobelts at depths of 0, 3, and 5 nm, respectively.

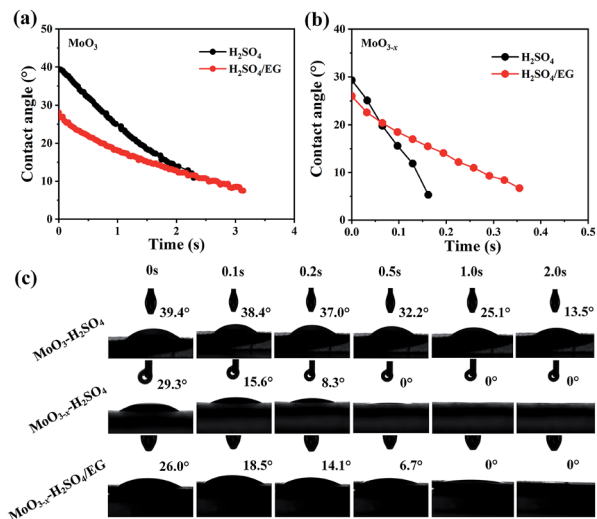


Fig. 5 (a) and (b) Wettability test results of the H₂SO₄ and H₂SO₄/EG electrolytes with MoO₃ and MoO_{3-x} nanobelts; (c) view of the contact angle of MoO₃-H₂SO₄, MoO_{3-x}-H₂SO₄ and MoO_{3-x}-H₂SO₄/EG at different times.

is displayed in Fig. 5, from which we can see that the infiltration speed of the H₂SO₄ and H₂SO₄/EG electrolytes in MoO_{3-x} nanobelts is much faster (about 10 times) than that in MoO₃ nanobelts (Fig. 5a and b). The H₂SO₄ and H₂SO₄/EG electrolytes need no more than 1.0 s to permeate MoO_{3-x} nanobelts (Fig. 5c). The excellent wettability of MoO_{3-x} nanobelts can be attributed to the increased interplanar

spacing, good dispersity and narrow structure of MoO_{3-x} nanobelts. This result demonstrated that the active sites in MoO_{3-x} nanobelts have a higher utilization and faster redox reaction. Good wettability ensures burst transmission of H⁺ in MoO_{3-x} nanobelts even under a large charge/discharge current density.

3.2 Electrochemical performance of the MoO_{3-x} nanobelt electrode for supercapacitors

As a contrast, MoO₃ nanobelts were tested in the H₂SO₄ electrolyte (labelled MoO₃-H₂SO₄). MoO_{3-x} nanobelts were tested in the H₂SO₄ and H₂SO₄/EG electrolytes (labelled MoO_{3-x}-H₂SO₄ and MoO_{3-x}-H₂SO₄/EG, respectively). The tests involving single electrodes mentioned above were carried out with a three-electrode system. Fig. 6a and S4-a† show the CV curves of MoO_{3-x}-H₂SO₄ and MoO₃-H₂SO₄ at scan rates from 2 to 100 mV s⁻¹, respectively, which are significantly different to some previous reports.^{41,42} The main reason is that the electrolyte used is different, which leads to different electrochemical reactions between MoO₃ and electrolyte ions. The shapes of their CV curves are thus quite different. Fig. S4-c† compares the differences of MoO_{3-x}-H₂SO₄ and MoO₃-H₂SO₄. Both of them have four pairs of redox peaks, which contribute a lot to the high specific capacitance. It can be seen that there are still obvious redox peaks even at a high scan rate of 100 mV s⁻¹, reflecting the fast H⁺ transmission and faradaic reaction. The CV curves of MoO₃-H₂SO₄ have a more evident polarization at high scan rates, showing a relatively rare poor capacity performance. All the oxidation peaks shift to a higher potential and

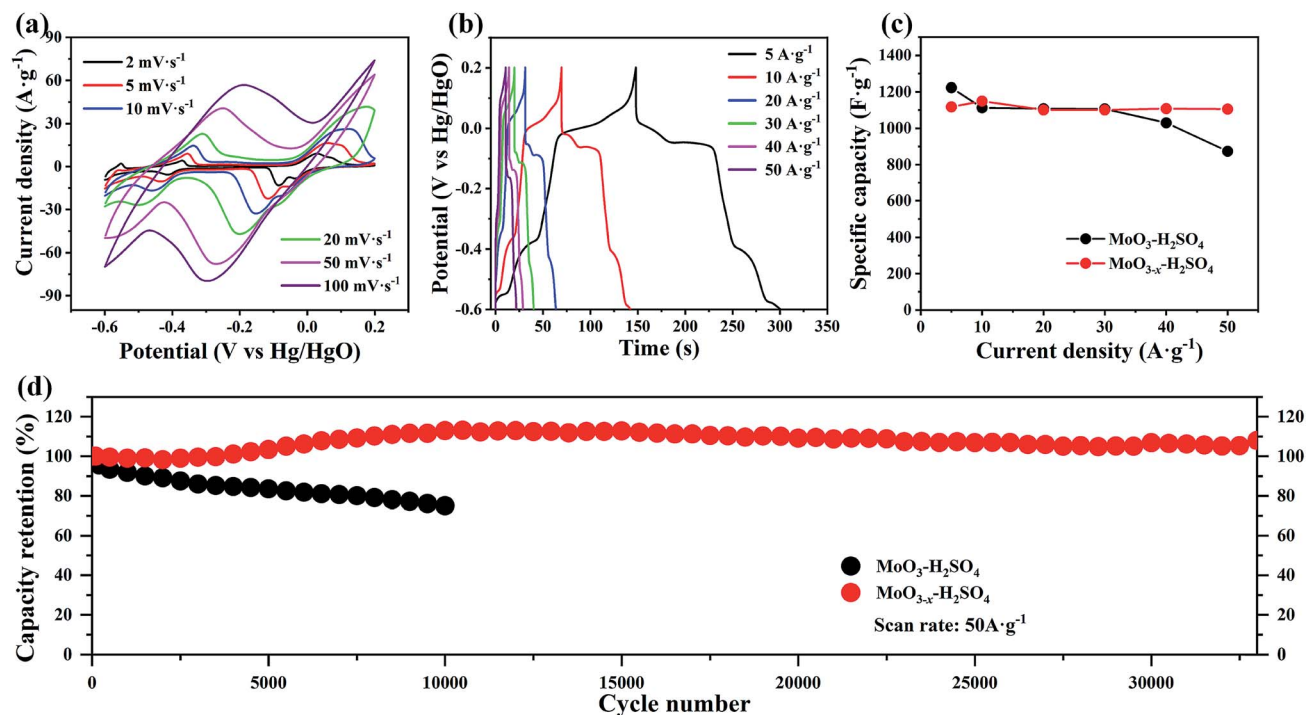


Fig. 6 (a) and (b) CV and GCD curves of MoO_{3-x}-H₂SO₄; (c) the specific capacitances of MoO₃-H₂SO₄ and MoO_{3-x}-H₂SO₄ at different current densities; (d) cycle performance of MoO₃-H₂SO₄ and MoO_{3-x}-H₂SO₄ at a high current density of 50 A g⁻¹.

reduction peaks shift to a lower potential when the scan rate is increased gradually, which may be due to the fact that transmission of H^+ cannot follow electron transport completely. As a result, the corresponding electrochemical reaction has a slight delay. GCD curves of $MoO_{3-x}-H_2SO_4$ and $MoO_3-H_2SO_4$ are shown in Fig. 6b and S4-b,† respectively. Four symmetric charge/discharge plateaus are observed clearly, corresponding to the four pairs of redox peaks in CV curves. EIS test results (Fig. S4-d†) show that MoO_{3-x} nanobelts have a lower resistance than MoO_3 , which derives from the microstructure of narrow nanobelts and masses of Mo^{4+} and Mo^{5+} inside MoO_{3-x} nanobelts. Fig. 6c shows the specific capacitance of $MoO_{3-x}-H_2SO_4$ and $MoO_3-H_2SO_4$ calculated from their GCD curves (Fig. 6b and S4-b,† respectively) at different current densities from 5 to 50 $A\ g^{-1}$. MoO_{3-x} nanobelts exhibit quite excellent rate capacity (98.9%), realizing a high specific capacitance of 1118 $F\ g^{-1}$ at a current density of 5 $A\ g^{-1}$ and can maintain 1106 $F\ g^{-1}$ when the current density increases to 50 $A\ g^{-1}$. However, MoO_3-

H_2SO_4 can only maintain 874 $F\ g^{-1}$ at a current density of 50 $A\ g^{-1}$. The excellent rate capacity and high specific capacitance of MoO_{3-x} nanobelts benefit a lot from the abundant Mo^{4+} and Mo^{5+} distributed uniformly in MoO_{3-x} nanobelts. The cycle stability of $MoO_3-H_2SO_4$ and $MoO_{3-x}-H_2SO_4$ was also evaluated by repeated charge/discharge at a high current density of 50 $A\ g^{-1}$. The test results are shown in Fig. 6d, from which it can be seen that MoO_{3-x} nanobelts have a much better cycle stability than MoO_3 nanobelts. The capacity retention of $MoO_3-H_2SO_4$ is just 75% after cycling 10 000 times. However, $MoO_{3-x}-H_2SO_4$ maintains a high capacity retention of 108% after cycling 33 000 times. The reason why the specific capacitance of $MoO_{3-x}-H_2SO_4$ increases may be the electrochemical activation process in the first thousand cycles. Obviously, introducing oxygen vacancies with uniform distribution has a large effect in improving the cycle stability. The integrated performance of the as-prepared MoO_{3-x} nanobelts is superior to that of all MoO_3- based materials researched before.^{20,25,27–32,34,43–45}

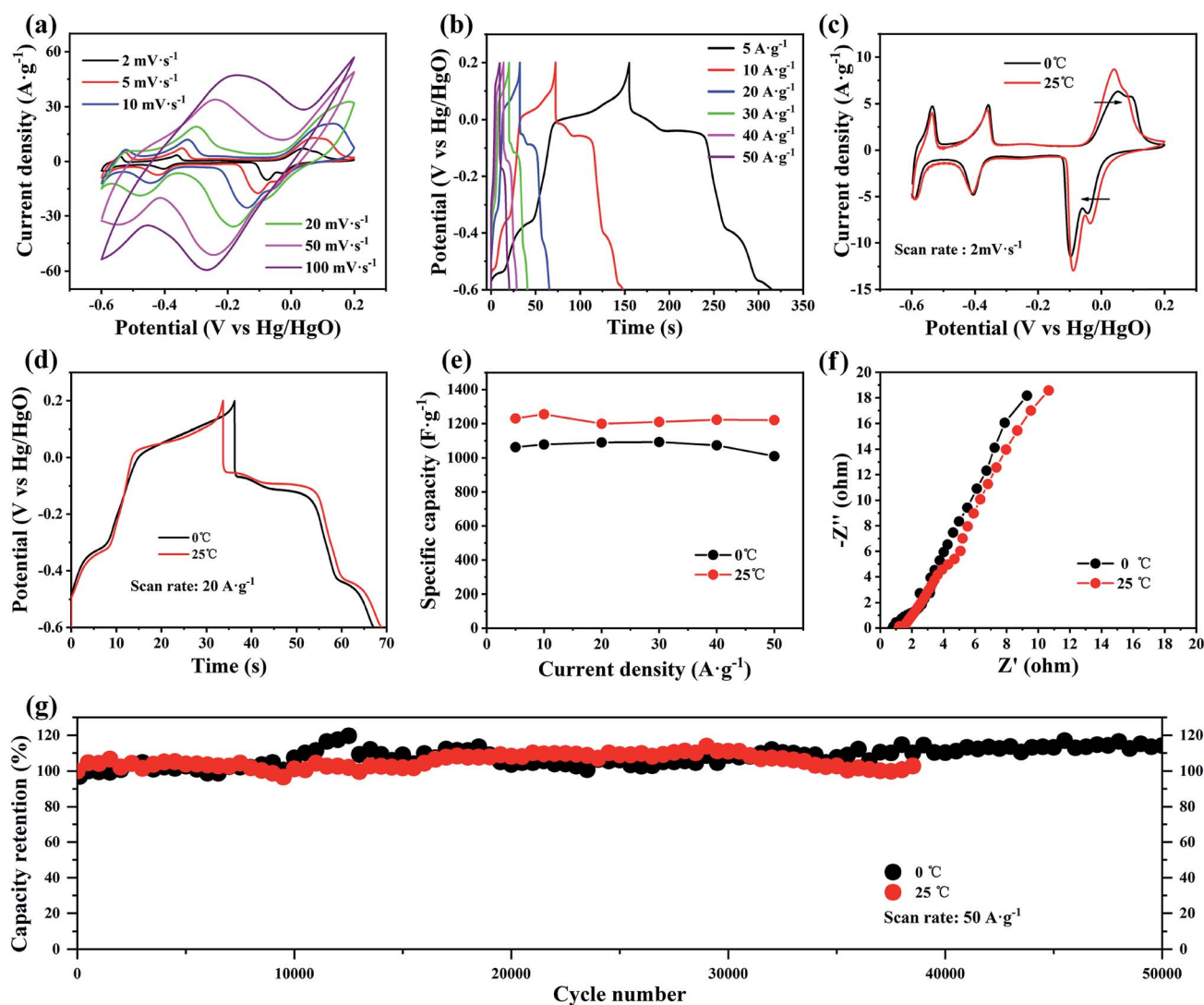


Fig. 7 (a) and (b) CV and GCD curves of $MoO_{3-x}-H_2SO_4/EG$; (c) and (d) comparison of CV and GCD curves of $MoO_{3-x}-H_2SO_4/EG$ at 0 and 25 $^{\circ}C$; (e) the specific capacitances of $MoO_{3-x}-H_2SO_4/EG$ at 0 and 25 $^{\circ}C$ from 5 to 50 $A\ g^{-1}$; (f) EIS test results of $MoO_{3-x}-H_2SO_4/EG$ at 0 and 25 $^{\circ}C$. (g) Cycle performance of $MoO_{3-x}-H_2SO_4/EG$ at 0 and 25 $^{\circ}C$.

The performance of MoO_{3-x} nanobelts (tested with the $\text{H}_2\text{SO}_4/\text{EG}$ electrolyte, labelled $\text{MoO}_{3-x}\text{-H}_2\text{SO}_4/\text{EG}$) was also measured at 0 and 25 °C (the lowest testing temperature for a single electrode is 0 °C because saturated KCl solution in the reference electrode may freeze below 0 °C). Fig. 7a and b show the CV and GCD curves of $\text{MoO}_{3-x}\text{-H}_2\text{SO}_4/\text{EG}$ at 25 °C. There is no significant difference compared to those of $\text{MoO}_{3-x}\text{-H}_2\text{SO}_4/\text{EG}$ at 0 °C (Fig. S5†), proving that MoO_{3-x} nanobelts exhibit good low-temperature performance. The redox peaks of $\text{MoO}_{3-x}\text{-H}_2\text{SO}_4/\text{EG}$ in the CV curve (scan rate: 2 mV s^{-1}) at 0 °C undergo a slight shift compared to those at 25 °C (Fig. 7c). This is because of the relatively slow H^+ transmission at low temperatures. Fig. 7d presents the GCD comparison of $\text{MoO}_{3-x}\text{-H}_2\text{SO}_4/\text{EG}$ at 0 °C and 25 °C at a current density of 20 A g^{-1} . Both of them have almost the same charge/discharge plateaus. The rate capacities of $\text{MoO}_{3-x}\text{-H}_2\text{SO}_4/\text{EG}$ at 0 °C and 25 °C are calculated from the GCD curves (Fig. S5-b† and 7b, respectively) and displayed in Fig. 7e. The specific capacitances of $\text{MoO}_{3-x}\text{-H}_2\text{SO}_4/\text{EG}$ at 25 °C are 1230 F g^{-1} and 1220 F g^{-1} at current densities of 5 A g^{-1} and 50 A g^{-1} , respectively, which almost approach the theoretical specific capacity of MoO_3 (1256 F g^{-1}) in a potential window of 0.8 V.⁴⁶ At 0 °C, its specific capacitance and rate capacity show a slight decrease but still maintain outstanding performance (1114 F g^{-1} at 5 A g^{-1} and 1008 F g^{-1} at 50 A g^{-1}). EIS (Fig. 7f) was carried out and the equivalent series resistance is less than $2\ \Omega$. In addition, the cycle stability of $\text{MoO}_{3-x}\text{-H}_2\text{SO}_4/\text{EG}$ was also tested with repeated charge/discharge at a current density of 50 A g^{-1} . The capacity retention is shown in Fig. 7g. There is no capacitance decay after cycling for 50 000 and 38 000 times at 0 and 25 °C, respectively. All the excellent performances mentioned above are closely related to the following reasons: (1) the ultrathin and narrow microstructure and good dispersity of MoO_{3-x} nanobelts shorten the migration distance of electrolyte ions, benefiting the utilization of active sites. (2) Abundant oxygen vacancies with uniform distribution inside MoO_{3-x} nanobelts contribute to increased concentration of carriers, resulting in faster reaction kinetics. (3) The excellent wettability of the $\text{H}_2\text{SO}_4/\text{EG}$ electrolyte ensures the rapid transmission of H^+ in MoO_{3-x} nanobelts, thus ensuring the full use of MoO_{3-x} nanobelts.

3.3 Electrochemical performance of the AC|| MoO_{3-x} asymmetric supercapacitor

To explore the practical application of the as-prepared oxygen vacancy-enriched MoO_{3-x} nanobelts, an asymmetric supercapacitor was assembled with active carbon (AC) as the anode, MoO_{3-x} nanobelts as the cathode and $\text{H}_2\text{SO}_4/\text{EG}$ as the electrolyte. Conductive carbon paper was selected to be the current collector of both the anode and cathode. Fig. 8a displays the CV curves of MoO_{3-x} nanobelts and AC electrodes at a scan rate of 10 mV s^{-1} , from which it can be seen that the faradaic pseudocapacitance of MoO_{3-x} nanobelts is much higher than the double-layer capacitance of AC. The voltage window of the supercapacitor can be extended effectively by combining pseudocapacitive and double-layer capacitive materials. Fig. 8b and c show the CV and GCD curves of the AC|| MoO_{3-x} asymmetric supercapacitor in different voltage windows to explore the most suitable voltage. When the voltage increases to 1.8 V, there is an evident phenomenon of polarization between 1.6 and 1.8 V. Thus, the most suitable voltage window is 0–1.6 V. The CV curves (Fig. 9a and c) show that there are several pairs of redox peaks corresponding to different pseudocapacitive reactions, keeping in line with the single MoO_{3-x} nanobelts electrode. The GCD curves at current densities from 1 to 50 A g^{-1} are exhibited in Fig. 9b. Charge/discharge plateaus are observed clearly even at a high current density of 50 A g^{-1} .

Moreover, the low-temperature performance of the AC|| MoO_{3-x} asymmetric supercapacitor was also tested at 0 °C and -25 °C . Fig. 9c compares the CV curves of the AC|| MoO_{3-x} asymmetric supercapacitor at different temperatures at a scan rate of 10 mV s^{-1} . The redox peaks have a higher potential at low temperatures, indicating slower response of redox reactions. The specific capacitance of the AC|| MoO_{3-x} asymmetric supercapacitor at different temperatures at current densities from 5 to 50 A g^{-1} is calculated from the GCD curves displayed in Fig. 9b, S6-b and S6-d.† The results are shown in Fig. 9d. At 25 °C, it is worth noting that the specific capacitance of the AC|| MoO_{3-x} asymmetric supercapacitor is higher at 2 A g^{-1} (346 F g^{-1}) than at 1 A g^{-1} (313 F g^{-1}). This can be accounted for by the electrochemical activation process at a small current

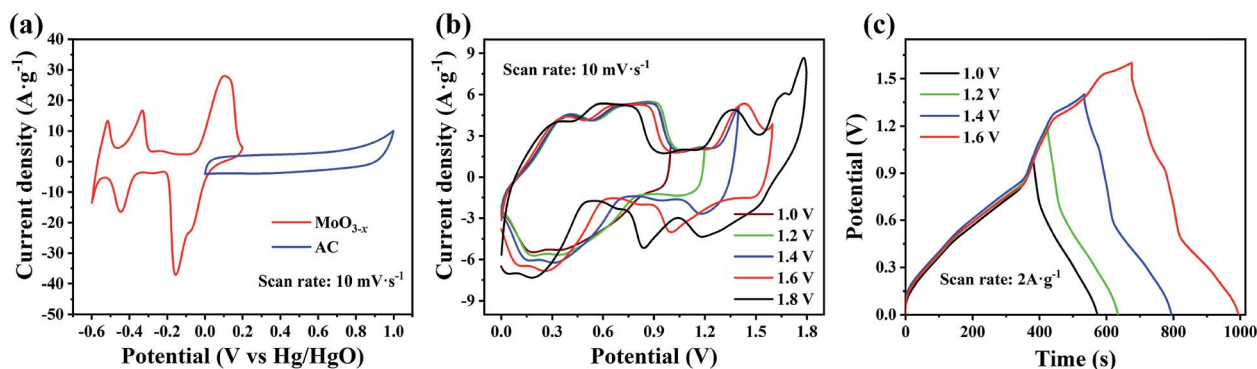


Fig. 8 (a) CV curves of MoO_{3-x} nanobelts and AC at a scan rate of 10 mV s^{-1} ; (b) and (c) CV and GCD curves of AC|| MoO_{3-x} in different voltage windows.

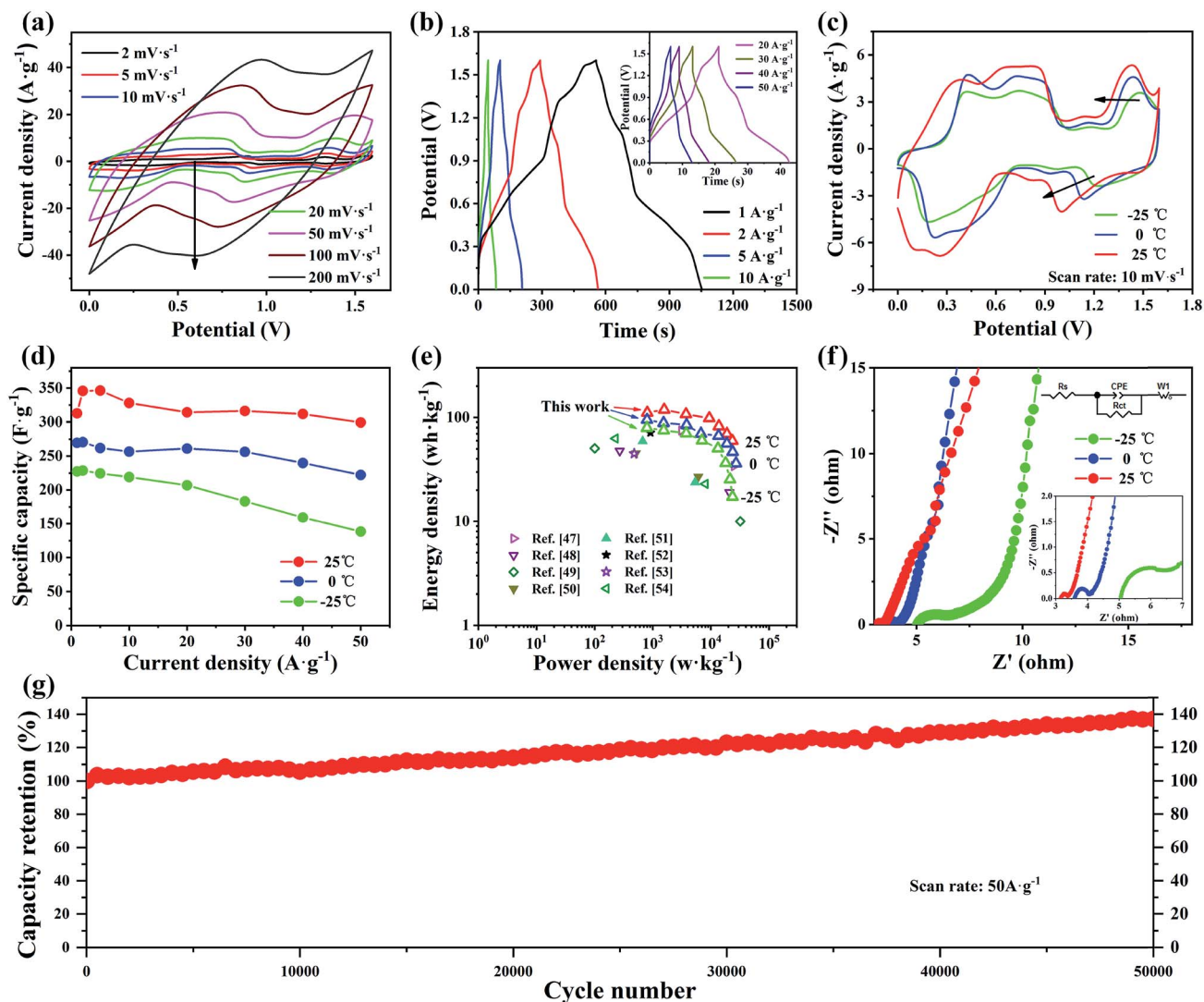


Fig. 9 (a) and (b) CV and GCD curves of AC||MoO_{3-x}; (c) comparison of CV curves of AC||MoO_{3-x} at different temperatures; (d) the specific capacitances of AC||MoO_{3-x} at different temperatures from 5 to 50 A g⁻¹; (e) Ragone plots of AC||MoO_{3-x} and other asymmetric supercapacitors; (f) EIS test results of AC||MoO_{3-x} at different temperatures and simulated model (inset). (g) Cycle performance of AC||MoO_{3-x} at 25 °C.

density. As the temperature decreases, the specific capacitance and rate capacity show a slight decline but are still excellent. At a high current density of 50 A g⁻¹, the AC||MoO_{3-x} asymmetric supercapacitor realizes a high specific capacitance of 299.4 F g⁻¹ at 25 °C and can maintain 222.3 F g⁻¹ and 138.4 F g⁻¹ at 0 °C and -25 °C, respectively. Based on the mass of active materials, the energy and power densities at different temperatures are calculated from the GCD curves (Fig. 9b, S6-b and S6-d†) and displayed in Fig. 9e. The as-prepared AC||MoO_{3-x} asymmetric supercapacitor shows a high energy density of 111 W h kg⁻¹ with a power density of 803 W kg⁻¹ and can maintain 50 W h kg⁻¹ at a superhigh power density of 27 321 W kg⁻¹, which are superior to most achievements reported previously (metal oxides/sulfide, carbon materials and their composites).⁴⁷⁻⁵⁴ Even at -25 °C, its energy and power densities remained at 80 W h kg⁻¹ and 794 W kg⁻¹ or 17 W h kg⁻¹ and 23 565 W kg⁻¹.

EIS tests of the AC||MoO_{3-x} asymmetric supercapacitor were also performed to evaluate the resistance (Fig. 9f). The fitting results are listed in Table 1. They demonstrate the small charge transfer resistance and high efficiency of fast electrode kinetics. It can be seen that the AC||MoO_{3-x} asymmetric supercapacitor has a small equivalent series resistance less than 5 Ω at different temperatures. In addition, we calculated the H⁺ diffusion coefficient with the following formula:

Table 1 Fitting results of AC||MoO_{3-x} obtained from the EIS curves at different temperatures and calculated D_{H^+}

Temperature/K	R_s/Ω	R_{ct}/Ω	$\sigma/\Omega \text{ s}^{-1/2}$	$D_{H^+}/\text{cm}^2 \text{ s}^{-1}$
248.15 (-25 °C)	4.99	1.23	2.54704	5.9×10^{-5}
273.15 (0 °C)	3.60	0.37	2.19592	8.4×10^{-5}
298.15 (25 °C)	3.17	0.18	1.75580	1.8×10^{-4}

$$D = \frac{R^2 T^2}{2A^2 n^4 F^4 C^2 \sigma^2} \quad (1)$$

where R and F are $8.314 \text{ J K}^{-1} \text{ mol}^{-1}$ and $96\,500 \text{ C mol}^{-1}$, respectively, T is the absolute temperature (K), A is the surface area of the electrode ($1 \times 10^{-4} \text{ m}^2$ in this work), n is 2, C is 2 mol L^{-1} (the H^+ concentration in the $\text{H}_2\text{SO}_4/\text{EG}$ electrolyte) and σ is the slope of the line $Z' \sim \omega^{-1/2}$ (Fig. S7†). The H^+ diffusion coefficients D ($\text{cm}^2 \text{ s}^{-1}$) at different temperatures were calculated and are listed in Table 1, from which we can see that the H^+ diffusion speeds at different temperatures are all very fast. The EIS test results indicate the outstanding performance of the AC|| MoO_{3-x} asymmetric supercapacitor from -25 to $25 \text{ }^\circ\text{C}$. Such excellent performance is accounted for the abundant oxygen vacancies with uniform distribution inside the MoO_{3-x} nanobelts, ultrathin and narrow microstructure and good infiltration of the $\text{H}_2\text{SO}_4/\text{EG}$ electrolyte.

In addition, cycle performance of AC|| MoO_{3-x} was tested by repeated GCD (current density: 50 A g^{-1}) and the results are shown in Fig. 9g. Interestingly, the capacity increased sustainably with the cycle number. After cycling 50 000 times, the capacity retention increases to 137%, exhibiting excellent cycle performance. The reasons may be explained as follows: on the one hand, with the increasing cycle number, the $\text{H}_2\text{SO}_4/\text{EG}$ electrolyte gradually permeates inside MoO_{3-x} nanobelts where there are numerous low valence Mo ions (Fig. 4). Electrochemical reactions between electrolyte ions and MoO_{3-x} nanobelts were carried out more completely. This process equals to the electrochemical activation process. On the other hand, the infiltration process of AC may play an important role in the sustainable increase of the capacitance of AC|| MoO_{3-x} . Fig. S8-a and S8-b† show the SEM images of AC under different magnification. It can be seen that the size is about several micrometers with good dispersity. Fig. S8-c† shows that the AC used in this work has a high specific surface area of $1986 \text{ m}^2 \text{ g}^{-1}$ and its pore diameter is less than 4 nm, which may result in a relatively slow speed of infiltration of the electrolyte. So, the reason why the specific capacitance increases sustainably along with the cycle number may be that AC was infiltrated gradually by the $\text{H}_2\text{SO}_4/\text{EG}$ electrolyte in the cycling process. The charge AC can store increases gradually, leading to the increase of the specific capacitance of AC|| MoO_{3-x} .

4. Conclusion

We have synthesized oxygen vacancy-enriched MoO_{3-x} nanobelts, which were prepared by a simple and low-cost one-step hydrothermal process with ethyl alcohol as the reductant. The as-prepared MoO_{3-x} nanobelts are very thin (30–40 nm) and narrow (100–200 nm), which is very beneficial for shortening the migration distance of electrolyte ions and improving the availability of active sites inside the MoO_{3-x} nanobelts. The oxygen vacancies were proved to distribute uniformly inside the MoO_{3-x} nanobelts and their concentration was calculated to be about 20% (equal to $\text{MoO}_{2.4}$), leading to faster reaction kinetics. Moreover, a new aqueous low-temperature $\text{H}_2\text{SO}_4/\text{EG}$ electrolyte was researched for the first time and it can tolerate a low

temperature of $-25 \text{ }^\circ\text{C}$. MoO_{3-x} nanobelts show excellent electrochemical performance in the $\text{H}_2\text{SO}_4/\text{EG}$ electrolyte at room temperature (1230 F g^{-1} and 1220 F g^{-1} at 5 A g^{-1} and 50 A g^{-1} , respectively, 100% after cycling 38 000 times). An AC|| MoO_{3-x} asymmetric supercapacitor was also assembled and it shows high energy densities of 111 W h kg^{-1} and 50 W h kg^{-1} at power densities of 803 W kg^{-1} and $27\,321 \text{ W kg}^{-1}$, respectively. Even at $-25 \text{ }^\circ\text{C}$, it realizes high specific capacitance, rate capacity, and high energy and power densities, exhibiting great potential for application in low-temperature environments. This work demonstrates that the oxygen vacancy-enriched ultrathin and narrow MoO_{3-x} nanobelts have great potential in the field of energy storage and conversion. It may prompt the study of vacancies in transition metal oxides/sulfides even in other materials.

Conflicts of interest

There are no conflicts of interest to declare.

Acknowledgements

This work was supported by the NSFC-Guangdong united fund (U1401246) and Shenzhen Basic Research Project (JCYJ20170817161127616).

Notes and references

- 1 M. Salanne, B. Rotenberg, K. Naoi, K. Kaneko, P. L. Taberna, C. P. Grey, B. Dunn and P. Simon, *Nat. Energy*, 2016, **1**, 16070.
- 2 A. S. Aricò, P. Bruce, B. Scrosati, J. M. Tarascon and S. W. Van, *Nat. Mater.*, 2005, **4**, 366–377.
- 3 L. L. Zhang and X. S. Zhao, *Chem. Soc. Rev.*, 2009, **38**, 2520–2531.
- 4 B. Housseinou, W. Wei, S. Pronkin, T. Romero, W. Baaziz, N.-D. Lam, C. Wei, O. Ersen and P.-H. Cuong, *Adv. Sustainable Syst.*, 2018, **2**, 1700123.
- 5 D. Y. Qu and H. Shi, *J. Power Sources*, 1998, **74**, 99–107.
- 6 Z. Lu, J. Foroughi, C. Wang, H. Long and G. G. Wallace, *Adv. Energy Mater.*, 2018, **8**, 1702047.
- 7 R. Huang, M. Huang, X. Li, F. An, N. Koratkar and Z.-Z. Yu, *Adv. Mater.*, 2018, **30**, 1707025.
- 8 Z. Zhang, C.-S. Lee and W. Zhang, *Adv. Energy Mater.*, 2017, **7**, 1700678.
- 9 M. Zou, W. Zhao, H. Wu, H. Zhang, W. Xu, L. Yang, S. Wu, Y. Wang, Y. Chen, L. Xu and A. Cao, *Adv. Mater.*, 2018, **30**, 1704419.
- 10 S. Iijima, *Nature*, 1991, **354**, 56–58.
- 11 F. Wang, X. Wu, X. Yuan, Z. Liu, Y. Zhang, L. Fu, Y. Zhu, Q. Zhou, Y. Wu and W. Huang, *Chem. Soc. Rev.*, 2017, **46**, 6816–6854.
- 12 P. Wang, Y. Xu, H. Liu, Y. Chen, J. Yang and Q. Tan, *Nano Energy*, 2015, **15**, 116–124.
- 13 Z. Lv, Y. Luo, Y. Tang, J. Wei, Z. Zhu, X. Zhou, W. Li, Y. Zeng, W. Zhang, Y. Zhang, D. Qi, S. Pan, X. J. Loh and X. Chen, *Adv. Mater.*, 2018, **30**, 1704531.

- 14 S. Kim, H. Jeong, J. Kwon, I. Ock, W. Suh, G. Stucky and J. Kang, *Energy Environ. Sci.*, 2014, **8**, 188–194.
- 15 H. Chen, L. Hu, Y. Yan, R. Che, M. Chen and L. Wu, *Adv. Energy Mater.*, 2013, **3**, 1636–1646.
- 16 X. Yang, H. Sun, P. Zan, L. Zhao and J. Lian, *J. Mater. Chem. A*, 2016, **4**, 18857–18867.
- 17 H. Tang, J. Wang, H. Yin, H. Zhao, D. Wang and Z. Tang, *Adv. Mater.*, 2015, **27**, 1117–1123.
- 18 E. G. da Silveira Firmiano, A. C. Rabelo, C. J. Dalmaschio, A. N. Pinheiro, E. C. Pereira, W. H. Schreiner and E. R. Leite, *Adv. Energy Mater.*, 2014, **4**, 1301380.
- 19 Z. Wang, Q. e. Zhang, S. Long, Y. Luo, P. Yu, Z. Tan, J. Bai, B. Qu, Y. Yang, J. Shi, H. Zhou, Z.-Y. Xiao, W. Hong and H. Bai, *ACS Appl. Mater. Interfaces*, 2018, **10**, 10437–10444.
- 20 Y. Liu, L. Li, J. Zhu, J. Xu, S. Liu, Y. Wang, C. Zhang and T. Liu, *J. Mater. Chem. A*, 2018, **6**, 13428–13437.
- 21 Y. Ma, C. Hou, H. Zhang, M. Qiao, Y. Chen, H. Zhang, Q. Zhang and Z. Guo, *J. Mater. Chem. A*, 2017, **5**, 14041–14052.
- 22 W. Zhao, Y. Li, S. Wu, D. Wang, X. Zhao, F. Xu, M. Zou, H. Zhang, X. He and A. Cao, *ACS Appl. Mater. Interfaces*, 2016, **8**, 34027–34033.
- 23 W. Raza, F. Ali, N. Raza, Y. Luo, K.-H. Kim, J. Yang, S. Kumar, A. Mehmood and E. E. Kwon, *Nano Energy*, 2018, **52**, 441–473.
- 24 B. You, N. Li, H. Zhu, X. Zhu and J. Yang, *Chemsuschem*, 2013, **6**, 474–480.
- 25 H. S. Kim, J. B. Cook, H. Lin, J. S. Ko, S. H. Tolbert, V. Ozolins and B. Dunn, *Nat. Mater.*, 2017, **16**, 454–462.
- 26 X. Hu, W. Zhang, X. Liu, Y. Mei and Y. Huang, *Chem. Soc. Rev.*, 2015, **46**, 2376–2404.
- 27 I. Shakir, M. Nadeem, M. Shahid and D. J. Kang, *Electrochim. Acta*, 2014, **118**, 138–142.
- 28 J. I. Hongmei and Y. Gang, *Adv. Funct. Mater.*, 2015, **25**, 1886–1894.
- 29 K. Zhou, W. Zhou, X. Liu, Y. Sang, S. Ji, W. Li, J. Lu, L. Li, W. Niu, H. Liu and S. Chen, *Nano Energy*, 2015, **12**, 510–520.
- 30 G. Saeed, S. Kumar, N. H. Kim and J. H. Lee, *Chem. Eng. J.*, 2018, **352**, 268–276.
- 31 F. Jiang, W. Li, R. Zou, Q. Liu, K. Xu, L. An and J. Hu, *Nano Energy*, 2014, **7**, 72–79.
- 32 X. Zhang, X. Zeng, M. Yang and Y. Qi, *ACS Appl. Mater. Interfaces*, 2014, **6**, 1125–1130.
- 33 X. Xiao, Z. Peng, C. Chen, C. Zhang, M. Beidaghi, Z. Yang, N. Wu, Y. Huang, L. Miao, Y. Gogotsi and J. Zhou, *Nano Energy*, 2014, **9**, 355–363.
- 34 T. Li, M. Beidaghi, X. Xiao, L. Huang, Z. Hu, W. Sun, X. Chen, Y. Gogotsi and J. Zhou, *Nano Energy*, 2016, **26**, 100–107.
- 35 Y. Li, D. Wang, Q. An, B. Ren, Y. Rong and Y. Yao, *J. Mater. Chem. A*, 2016, **4**, 5402–5405.
- 36 Q.-L. Lu, S.-X. ZHAO, C.-K. Chen, X. Wang, Y.-F. Deng and C. Nan, *J. Mater. Chem. A*, 2016, **4**, 14560–14566.
- 37 S. Balendhran, J. Deng, J. Z. Ou, S. Walia, J. Scott, J. Tang, K. L. Wang, M. R. Field, S. Russo, S. Zhuiykov, M. S. Strano, N. Medhekar, S. Sriram, M. Bhaskaran and K. Kalantar-zadeh, *Adv. Mater.*, 2013, **25**, 109–114.
- 38 X. K. Hu, Y. T. Qian, Z. T. Song, J. R. Huang, R. Cao and J. Q. Xiao, *Chem. Mater.*, 2008, **20**, 1527–1533.
- 39 G. Wang, Y. Ling and Y. Li, *Nanoscale*, 2012, **4**, 6682–6691.
- 40 M. Dieterle, G. Weinberg and G. Mestl, *Phys. Chem. Chem. Phys.*, 2002, **4**, 812–821.
- 41 L. Huang, B. Yao, J. Sun, X. Gao, J. Wu, J. Wan, T. Li, Z. Hu and J. Zhou, *J. Mater. Chem. A*, 2017, **5**, 2897–2903.
- 42 J. Yang, X. Xiao, P. Chen, K. Zhu, K. Cheng, K. Ye, G. Wang, D. Cao and J. Yan, *Nano Energy*, 2019, **58**, 455–465.
- 43 P. Duy Van, R. A. Patil, C.-C. Yang, W.-C. Yeh, Y. Liou and Y.-R. Ma, *Nano Energy*, 2018, **47**, 105–114.
- 44 V. Kumar, X. Wang and P. S. Lee, *Nanoscale*, 2015, **7**, 11777–11786.
- 45 B. Yao, L. Huang, J. Zhang, X. Gao, J. Wu, Y. Cheng, X. Xiao, B. Wang, Y. Li and J. Zhou, *Adv. Mater.*, 2016, **28**, 6353–6358.
- 46 T. Brezesinski, J. Wang, S. H. Tolbert and B. Dunn, *Nat. Mater.*, 2010, **9**, 146–151.
- 47 T. Zhai, S. Sun, X. Liu, C. Liang, G. Wang and H. Xia, *Adv. Mater.*, 2018, **30**, 1706640.
- 48 Y. Wang, W. Lai, N. Wang, Z. Jiang, X. Wang, P. Zou, Z. Lin, H. J. Fan, F. Kang, C.-P. Wong and C. Yang, *Energy Environ. Sci.*, 2017, **10**, 941–949.
- 49 H. Xia, C. Hong, B. Li, B. Zhao, Z. Lin, M. Zheng, S. V. Savilov and S. M. Aldoshin, *Adv. Funct. Mater.*, 2015, **25**, 627–635.
- 50 L. Shen, J. Wang, G. Xu, H. Li, H. Dou and X. Zhang, *Adv. Energy Mater.*, 2015, **5**, 1400977.
- 51 H. Li, Y. Gao, C. Wang and G. Yang, *Adv. Energy Mater.*, 2015, **5**, 1401767.
- 52 K. M. Hercule, Q. Wei, O. K. Asare, L. Qu, A. M. Khan, M. Yan, C. Du, W. Chen and L. Mai, *Adv. Energy Mater.*, 2015, **5**, 1500060.
- 53 T. Zhai, X. Lu, Y. Ling, M. Yu, G. Wang, T. Liu, C. Liang, Y. Tong and Y. Li, *Adv. Mater.*, 2014, **26**, 5869–5875.
- 54 C. Long, D. Qi, T. Wei, J. Yan, L. Jiang and Z. Fan, *Adv. Funct. Mater.*, 2014, **24**, 3953–3961.